FISEVIER

Contents lists available at ScienceDirect

Additive Manufacturing

journal homepage: www.elsevier.com/locate/addma



Research paper



Layer time optimization in large scale additive manufacturing via a reduced physics-based model $^{\!\!\!\!\!\!\!\!/}$

Lu Liu a,1 , Eonyeon Jo b,1 , Dylan Hoskins c , Uday Vaidya d,e,f , Soydan Ozcan f , Feng Ju a,* , Seokpum Kim b,f

- a School of Computing and Augmented Intelligence, Arizona State University, Tempe, AZ, United States of America
- b The Bredesen Center, University of Tennessee, Knoxville, TN, United States of America
- ^c Haddy, Inc., St. Petersburg, FL, United States of America
- d Department of Mechanical, Aerospace, and Biomedical Engineering, University of Tennessee, Knoxville, TN, United States of America
- e Institute for Advanced Composites Manufacturing Innovation (IACMI), Knoxville, TN, United States of America
- f Manufacturing Science Division, Oak Ridge National Laboratory, Oak Ridge, TN, United States of America

ARTICLE INFO

ABSTRACT

Keywords:
Large scale additive manufacturing
Physics-based model
Layer time optimization

In large-scale additive manufacturing (AM), ensuring product quality and production efficiency has been dependent on the skills and experiences of machine operators, and there has been a lack of guidelines based on accurate data and a model from systematic analyses. The product quality and the production efficiency are highly influenced by layer deposition time (a.k.a. layer time). The determination of a proper layer time involving a high-fidelity model requires high computational cost, and cannot be utilized for an online feedback system where fast temperature prediction is necessary. In this work, we propose a fast layer time optimization framework utilizing a reduced physics-based one-dimensional heat transfer model to predict the cooling behavior and layer temperature. We also perform a high-fidelity three-dimensional finite element analysis (FEA) with two geometries involving large angles and sharp angles. The temperature from the reduced model is adjusted by variances calibrated based on the FEA model reflecting geometric effect so that the prediction from the reduced model can be applied to complex geometric designs. This process of temperature prediction is named the hybrid model, and it allows the offline design of layer time optimization. We combine the temperature data into an optimization model, which monitors the temperature of multiple positions and balances the relationship between the layer time and the layer temperature. We also develop an iterationbased solution approach by combining the layer time optimization model with the hybrid model. The approach involves iterations between the proposed layer time from the optimization model and the temperature predicted from the hybrid model until the predicted temperature converges to a target layer temperature, determining an optimal layer time. We apply the developed process to two cases with different printing geometries: hexagon and star shapes. This paper provides a simplified and lower-cost methodology to determine an optimal layer time and improve product quality in the large-scale AM process.

1. Introduction

Additive Manufacturing (AM) can be defined as a "layer-based automated fabrication process for making scaled 3-dimensional(3D)

physical objects directly from 3D computer-aided design (CAD) data without using part-depending tools [1]". It is also known as 3D printing, and it has been widely used to fabricate complex geometries in

E-mail address: fengju@asu.edu (F. Ju).

Notice of Copyright: This manuscript has been authored by UT-Battelle, LLC, under contract DE-AC05-000R22725 with the US Department of Energy (DOE). The US government retains and the publisher, by accepting the work for publication, acknowledges that the US government retains a non-exclusive, paid-up, irrevocable, world-wide license to publish or reproduce the submitted manuscript version of this work or allow others to do so, for US government purposes. DOE will provide public access to these results of federally sponsored research in accordance with the DOE Public Access Plan (http://energy.gov/downloads/doe-public-access-plan).

^{*} Corresponding author.

¹ The two authors contributed equally to this paper.

Too long layer time Over cooling Debonding, Crack, Warpage Too short layer time Over heating Collapse Collapse

Fig. 1. (Center) Failure cases in Big-Area Additive Manufacturing (BAAM) process due to improper temperature control and (Left) a photograph of the failure from interlayer debonding due to over-cooling [6] and (Right) a photograph of the failure from material collapse due to over-heating.

the aerospace and automotive industry. The main developed methods include extrusion deposition process, powder bed fusion, inkjet printing, stereolithography, direct energy deposition, and laminated object manufacturing. Metals, polymers, ceramics, and concrete, as common materials, are used in the process of additive manufacturing [2].

In a large-scale polymer extrusion system, a granular or pelletized polymer with a screw-type extruder, which is used in the traditional extrusion manufacturing process, is used for a feeding system [3]. In the feeding system, the screw in the extruder generates pressure and heat during the melting of the feedstock. The pressure allows the melted substrate to flow throughout the print nozzle. Large-scale additive manufacturing systems with thermoplastic use a combination of the polymer extrusion system and a deposition system to liquefy the feedstock and deposit the molten substance for building a largescale structure layer by layer [4]. LSAM® by Thermwood is an example of a large-scale additive manufacturing system. The LSAM® system allows the extruded deposition of polymer materials at the rate of up to 227 kg/h for large-scale structures. The system has a 40 mm print head, and it supports producing parts 30.4 m long, 3.0 m wide, and 1.5 m high by using a thermoplastic pellet form feedstock [5]. This commercially available large-scale 3D printer contributes to manufacturing with the benefits of cost-effective production and design freedom.

One of the major challenges with such large-scale printers is determining an optimal layer deposition time since the prediction of the temperature change during the process is not trivial due to a large amount of deposited material with an arbitrary shape and size. An overcooled surface from too long layer deposition time (a.k.a. layer time) will cause interlayer debonding, cracking, and warping. Conversely, an over-heated surface from too short layer time will experience material collapse due to the lack of stiffness when new layers are deposited [7]. Fig. 1 shows these two types of failure cases from Big Area Additive Manufacturing (BAAM) due to the improper layer times, which are also typically shown across various types of large-scale extrusion deposition systems. Layer time has a crucial impact on the internal stresses and ultimate deformation of printed products with different thermal gradients [8]. Therefore, in order to prevent these failures during the large-scale additive manufacturing process, an optimal layer time should be determined, considering product quality and production

In previous studies, a real-time control model is developed to determine an optimal layer time and improve both product quality and production efficiency [9]. In the model, the layer time is controlled with the print surface temperature captured by infrared cameras during the entire process. However, real-time temperature data is expensive and inflexible because experiments should be repeated when printing conditions change. Another alternative approach to getting temperature history data is the finite element analysis (FEA) based simulation, which is more flexible with different geometries, but the model is computationally expensive [10].

Instead of using expensive experimental printing data and timeconsuming FEA-based simulations, this paper intends to generate temperature prediction data by applying a reduced physics-based model for a given layer time. This study develops a 1D heat transfer model, considering conduction, natural convection, and radiation. Since the developed model assumes a simple wall geometry, the model cannot capture the geometry-dependent cooling effect. In order to handle the effect of various geometries, temperature variances for each position in the local cooling duration are extracted from the FEA-based simulation. Then, the cooling temperature data given by the physics-based model is added with the corresponding variances to simulate different cooling curves for each position on the layer. A layer time optimization model is developed to determine the optimal layer time for the printing process by considering the trade-offs between temperature deviation and production efficiency. Two cases with hexagon and star geometries are used in this study. Besides the benefits of quality control and efficiency improvement, this study can provide a more simplified and cost-effective tool for the large-scale additive manufacturing process. The proposed method focuses on homogeneous single-bead print with constant width and height for manufacturing simple geometries. Approaches, which apply to more complicated geometries, will be considered in future work.

The paper is structured as follows. Relevant pieces of literature are reviewed in Section 2. Section 3 shows the material characterization and the two geometries printed from LSAM®. The FEA-based simulation and the reduced physics-based model for temperature prediction are introduced in Section 4, and the optimal layer time control is provided in Section 5. 6 presents two tested cases based on different geometries. Finally, conclusions and future work are summarized in Section 7.

2. Literature review

The characteristics of the final product, such as dimensional accuracy, better mechanical properties, and reduced deformation, highly depend on the process parameters of the extrusion deposition process. Mohan et al., [11] reviewed various studies on the optimization of process parameters for quality characteristics of the extrusion deposition process. Studies have been conducted on the process parameter optimization such as layer thickness [12,13], the diameter of the nozzle, temperature evolution, temperature of extrusion, raster orientation [14], and raster angle and raster gap [15] during the extrusion deposition process. These studies focused on verifying the relationship between different process parameters and the corresponding effects on the final product. Other studies focused on the relationship between print quality and the surface temperature during the whole process [16-18]. Thermal cameras were used to measure the extruder head and extruded substance temperature at the moment of deposition in the polymer AM process [19]. A recent study [8] suggests that warping and cracking occur as the print surface temperature goes below the glass transition temperature.

Online layer time control models were developed to improve print quality and prevent failure [9,20]. In the control models, thermal images were gathered by IR cameras to measure the surface layer temperature. The temperature data were used in their feedback system to determine an optimal layer time. The adjusted layer time ensured the proper surface layer temperature when a new layer was deposited. In the process of determining the optimal layer time, a regression model was used to predict the layer temperature before a new layer was deposited. The regression model utilized the temperature data from experiments with a constant layer time, so the model was not flexible enough to be applied to various scenarios with different manufacturing conditions. An advanced optimization model was proposed to enhance its applicability [21], considering the effect of various layer time cases. The model improved the printing efficiency, but it still needs a large amount of experimental data.

The simulations of the extrusion deposition process utilize a progressive element activation technique, in which the initially inactive elements are activated with the printing head movement (tool path). In a large-scale extrusion deposition process, the large deposition beads and high deposition rate produce large thermal mass and residual heat, which then leads to residual stresses during cooling, causing warping and delamination between deposited layers. Therefore, the accurate prediction of temperature (i.e., residual heat) is important to minimize the warpage and optimize the printing process. FEA simulation has often been used to predict the temperature evolution in the extrusion deposition process [22-24]. In our previous study [10], surface layer temperature in LSAM® was predicted via FEA simulation with the progressive element activation. With the predicted surface layer temperature, the optimal control approach in Ref. [9] was used to optimize the layer time [10]. Typically, performing simulation is less expensive than large-scale additive manufacturing; nevertheless, a high-fidelity complex simulation model is still time-consuming. If a layer time optimization algorithm requires multiple iterations of simulations with different layer times, then the time it takes to obtain an optimal layer time will be determined by an individual simulation run time.

A reduced 1D thermal model was developed to simulate the thermal history for the large-scale thermoplastic AM process is developed [8], and the model predicted layer temperatures that are in excellent agreement with the observed temperatures from corresponding experiments. The printed wall is assumed to have a large length compared to width and thickness (Biot number $\ll 1$) for the 1D heat transfer condition. Also, a 2D finite volume model is developed with 2D spatial discretization to simulate the heat transfer during the large-scale additive manufacturing process [25]. Inspired by the aforementioned studies, we developed a simplified physics-based activation model to predict the temperature change in additive manufacturing. Then, an adjusted optimal control model is practiced to generate the best optimal layer time, which can be used to ensure both product quality and production efficiency. This method avoids applying large amounts of costly experimental or high-fidelity simulation data, and it provides reasonable results.

3. Experiments

3.1. Material characterization

In our previous study [26], tensile tests were conducted to investigate the relationship between the layer temperature and the interlayer bonding property. Single bead wall hexagon structures were fabricated in the LSAM® system using carbon fiber reinforced polycarbonate (CF/PC) with different layer times — 140, 200, 260, and 320 s. The corresponding layer temperatures from the four-layer times (140, 200, 260, and 320 s) were 140 °C, 120 °C, 104 °C, and 89 °C, respectively. The layer time was changed by modifying the waiting time (i.e., parking time of the nozzle) while maintaining the printing time (i.e., deposition time with nozzle movement). The layer time is the

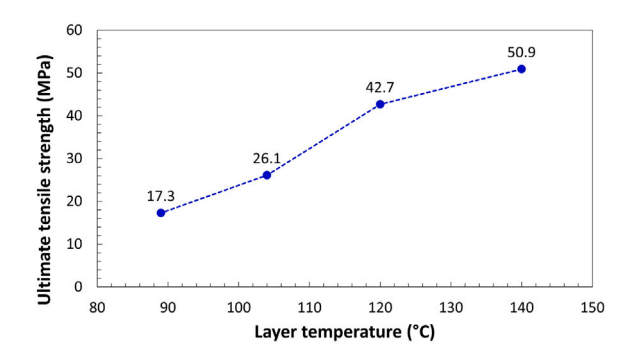


Fig. 2. Effect of layer temperature on the tensile strength of printed part fabricated by LSAM® system. Y-axis in the figure is the ultimate tensile strength in the stacking direction [26].

time from the deposition moment of a layer until the subsequent layer is deposited on top of the previous layer (i.e., layer time = waiting time + printing time). Also, in this work, we define layer temperature as the temperature of the top layer right before the next top layer is deposited (i.e., the temperature of the top layer after the layer time had passed). Therefore, a long layer time corresponds to a low layer temperature because the layer takes a long time to cool down. Tensile test specimens were fabricated from the printed hexagon structures in the stacking direction to measure the interlayer bonding strength. The effect of layer temperature on the tensile strength in the stacking direction is shown in Fig. 2 [26]. The interlayer strength increased when the layer temperature reached 140 °C, indicating a substantial association between the layer temperature and the interlayer strength. The experiment results align well with previous research, which shows the relationship between the layer temperature and the interlayer bonding property in a large-scale extrusion deposition system [27]. Furthermore, the tensile strength in the stacking direction exhibited continuous improvement until the layer surface temperature reached the glass transition temperature. However, excessive overheating can lead to polymer degradation and successive material collapse [28].

Dynamic mechanical analysis (DMA) was conducted to measure the glass transition temperature, and the result is shown in Fig. 3(a). The DMA result shows the glass transition temperature of 145 °C [26], which is the layer temperature at the upper limit of the interlayer bonding strength in Fig. 2. Therefore, the glass transition temperature can be a target layer temperature in the large-scale additive manufacturing process. When the layer temperature is 20 °C higher than the glass transition temperature, the printed structure collapses due to the lack of stiffness. Considering the deposited polymer material should be solidified to ensure enough stiffness, the upper limit of the layer temperature should be 165 °C. Conversely, when the layer temperature is 20 °C lower than the glass transition temperature, the tensile strength rapidly decreases in the interlayer bonding test. Throughout these experimental results, our layer temperature window during the optimization process is determined between 125 °C (lower limit) and 165 °C (upper limit).

Heat capacity was measured [26] as a function of temperature for CF/PC based on the American Society for Testing and Materials (ASTM) E1269 standard [29], and Fig. 3(b) shows the test result. The heat capacity was measured by differential scanning calorimetry (DSC) under an inert atmosphere and with sapphire as the reference material. In this study, we adopt the material properties in Fig. 3 (b). Piecewise linear regression is used to describe the change of heat capacity with temperature (red dashed line), and it is used in the FEA simulation and the reduced 1D model.

3.2. Sample printing in large-scale additive manufacturing

Hexagon and star shape geometry parts with single bead walls are designed and fabricated with different layer times, using the LSAM $^{\circledR}$

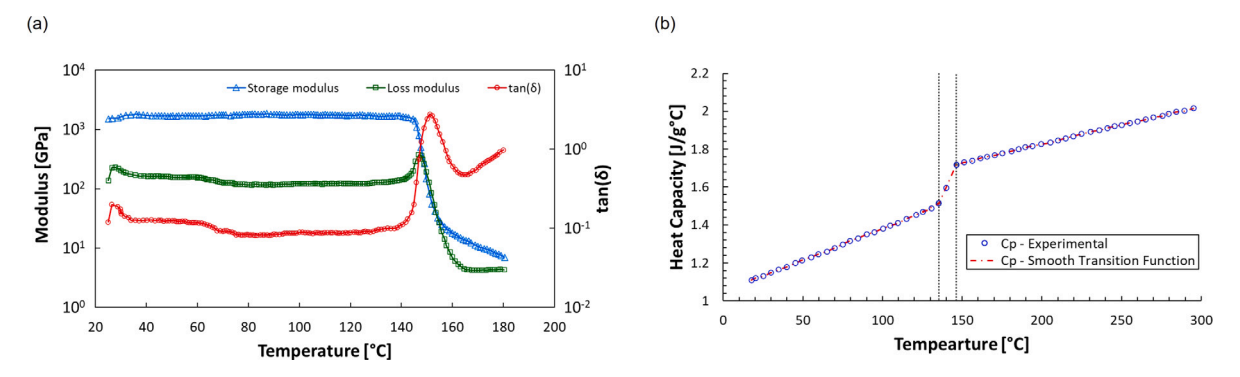


Fig. 3. Material property measurements with CF/PC (a) DMA result for the glass transition temperature [26] and (b) DSC results for the heat capacity as a function of temperature [26].

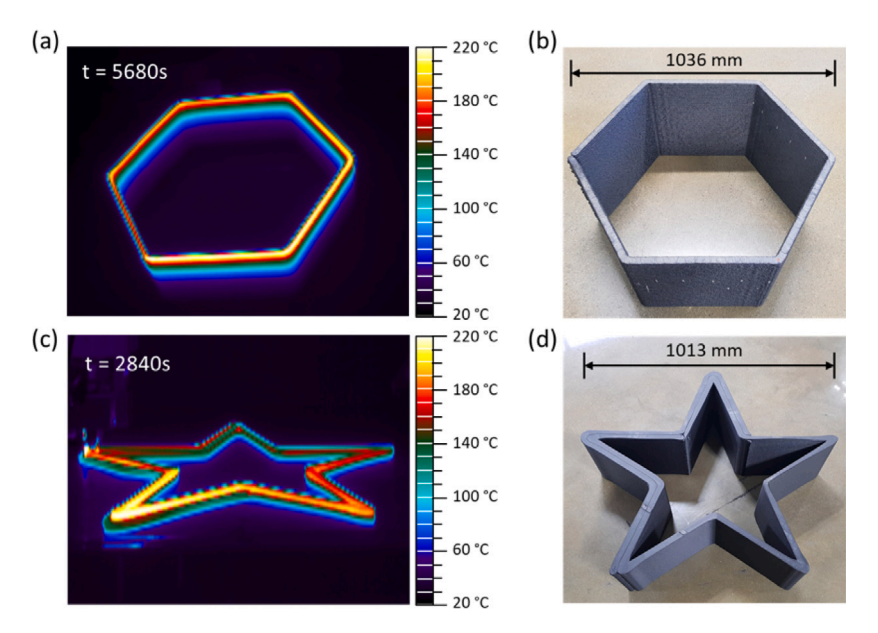


Fig. 4. Snapshots of temperature field captured from the IR camera (a), (c), and photographs of the printed structures (b), (d), for the hexagon shape print and the star shape print.

system. The parts have a 1 m length and 0.3 m height with 61 layers. The printing parameters such as extrusion temperature, bed temperature, ambient temperature, bead height, and bead width are shown in Table 1. The material used in experiments is polycarbonate reinforced with 20% carbon fiber by weight (CF/PC). Thermal images are gathered via an infrared (IR) camera during the entire LSAM® process. Fig. 4(a) and (b) show a snapshot of the temperature field from the IR camera during the printing of the hexagon shape structure and a photograph of the fabricated structure. Also, Fig. 4(c) and (d) show a snapshot of the temperature field from the IR camera during the printing of the star shape structure and a photograph of the fabricated structure. Temperature data are extracted from the IR thermal images. Temperature history and cooling behavior during the LSAM® process are investigated from the temperature data. Also, the temperature data during the entire process are used to verify the results of the FEA simulation and the reduced 1D model.

4. Temperature profile prediction

4.1. FEA simulation

Finite element analysis (FEA) is used in the AM process simulation to investigate temperature profiles and layer temperature. In the FEA simulation, heat transfer occurs by conduction, convection, and radiation. The manufacturing process and heat transfer mechanisms

 Table 1

 Experimental conditions for the large-scale 3D printing.

Value
265
30
30
5.08
20.32
90, 140, 200
200

are shown in Fig. 5. The CF/PC used material exhibits anisotropic thermal properties due to the presence of reinforced carbon fibers. The addition of carbon fibers increases the thermal conductivity of the composite along the fiber direction [30]. Thus, fiber orientation should be considered to simulate the manufacturing process.

The three-dimensional Fourier's law governs the anisotropic thermal conductivity with three conductivity parameters (κ_{11} , κ_{22} , κ_{33}) for the x, y, and z directions. Considering that the reinforced fibers are aligned along the tool path direction, the principal direction (x-direction) for the material is chosen as the deposition direction, and the z-direction is chosen as the stacking direction. The conductivity values are measured in previous research for the used material with the same large-scale material deposition system [26]. The values are the product of the thermal

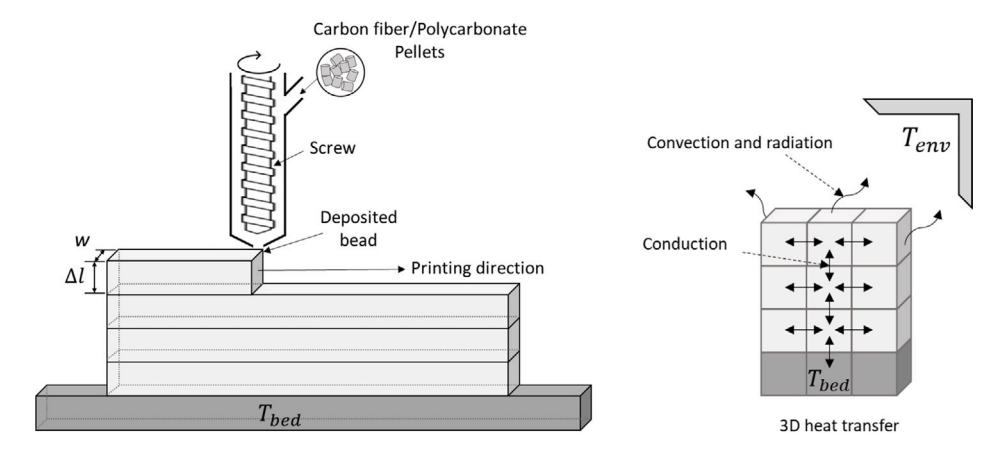


Fig. 5. Schematic of the large-scale additive manufacturing process with polymer extrusion and heat transfer via conduction, convection, and radiation in the 3D FEA model.

Table 2
FEA simulation Input parameters.

The Property of the Control of the C	
Variable name	Value
Thermal conductivity at T_g , κ_{11} , κ_{22} , κ_{33} [W/m K]	0.77, 0.35, 0.27
Density, ρ [kg/m ³]	1470
Convection coefficient, h_{cv} [W/m ² K]	4
Emissivity, ϵ	0.9
Stefan–Boltzmann constant, σ [W/m ² K ⁴]	5.67×10^{-8}
Deposition temperature, T_{dep} [°C]	210
Ambient temperature, T_{env} [°C]	30
Bed temperature, T_{bed} [°C]	50
Layer Height, 41, [mm]	5.08
Thickness, w, [mm]	20.32

diffusivity, the heat capacity, and the density in piecewise functions of temperature. The piecewise functions are used in the FEA simulation. Newton's law of cooling with a constant heat transfer coefficient is used for the natural convection (h_{cv}). The convection coefficient is calibrated by comparing the cooling behavior of the printed substance between the experiment and the simulation. Thermal radiation is governed by the Stefan–Boltzmann law with a constant emissivity (σ). The emissivity is calibrated by comparing the temperature of extruder measured by thermocouple and the temperature of extruded material measured by IR thermal image. We determine the emissivity when the thermal IR data shows the same temperature as the extrusion temperature. The used material property values in FEA simulation are summarized in Table 2.

In the FEA model, the spatial and temporal domains during the deposition process are discretized into finite elements (DC3D8, linear heat transfer brick with eight nodes) and time steps (1 step = 5 s), respectively. To implement the layer-by-layer deposition process, the elements are generated with the height of a printed layer (height = 5.08 mm). When the tool path passes through the element, the element is activated, and the boundary conditions are concurrently updated over the entire simulation. The progressive material activation technique is used to imitate the additive manufacturing process, and the progressive deposition process is shown in Fig. 6(c). The temperature profiles from simulations and experiments for the hexagon prints at different process times are compared, and the results are shown in Fig. 6(d). The temperature profiles are recorded from the base to the top surface at the wall and the angle positions. The solid lines correspond to the simulation results, while the dashed lines represent the experimental results. The red and blue lines show the temperature profile at the wall and angle, respectively. During the printing process in the experiments, there is a temperature discrepancy between the wall and the angle positions. The material at the corner (i.e., at the angled position) cools faster than the material at the wall position. It is because the material at the corner has a larger surface area on the outside

surface than the inside surface. The difference in surface area between the inside and the outside surface will be more significant if the corner becomes sharper (i.e., smaller angle); hence higher temperature discrepancy is expected for sharper geometries between the angled position and the wall position. The temperature discrepancy due to the angle is accurately captured in the simulation. Despite the complexity of the printing, the simulation results show a good agreement with experiments, illustrating the reliability of the numerical simulations in predicting the layer temperature.

4.2. Finite differential model with node activation (1D model)

A reduced physics-based model is developed to predict the temperature history, substituting the time-consuming FEA simulations. A schematic of the large-scale AM process and 1D heat transfer boundary conditions are shown in Fig. 7. In the finite differential model, heat transfer occurs by thermal conduction, natural convection, and radiation. The model assumes that the deposited single bead wall has infinite length and a constant width (w), and layer height (Δl) . In this condition, the Biot number (=0.1818), which shows the ratio of convection to conduction, suggests that thermal equilibration via conduction is faster than the rate of heat loss due to convection at the surface. Also, in the condition, the temperature is assumed to be uniform in the through-thickness direction so that conduction only occurs in the vertical direction [8]. Therefore, the model assumes that there are no thermal gradients along the length and width direction of the printed wall, indicating that heat conduction only occurs in the vertical (1D) direction. A node is activated with time increment, updating the boundary conditions, like a new layer is built during the AM process. The time increment is defined by the layer time (Δt). At the upper surface of a top layer and the sides of all layers, free surfaces experience natural convection and radiation to the environment at temperature (T_{env}). The bottom layer experiences conduction with a constant temperature boundary condition of the bed (T_{hed}) . The relevant material properties used in this model are specific heat capacity(C_n), density (ρ), thermal conductivity (κ), natural convection coefficient (h_{cv}), Stefan–Boltzmann constant (σ), and emissivity (ϵ). The material property values are summarized in Table 3. The heat capacity changes corresponding to the temperature during the heat transfer

The 1D partial differential equation that describes heat transfer in the printed layers is,

$$\rho c_p w \Delta l \frac{dT}{dt} = k w \Delta l \frac{\partial^2 T}{\partial l^2} - Q_{out}$$
 (1)

$$Q_{out} = \epsilon \sigma A(T(l,t)^4 - T_{env}^4) + h_{cv} A(T(l,t) - T_{env})$$
(2)

where T is temperature, t is time, and A is area of the free surface. We assume there is no energy generation within the material. The

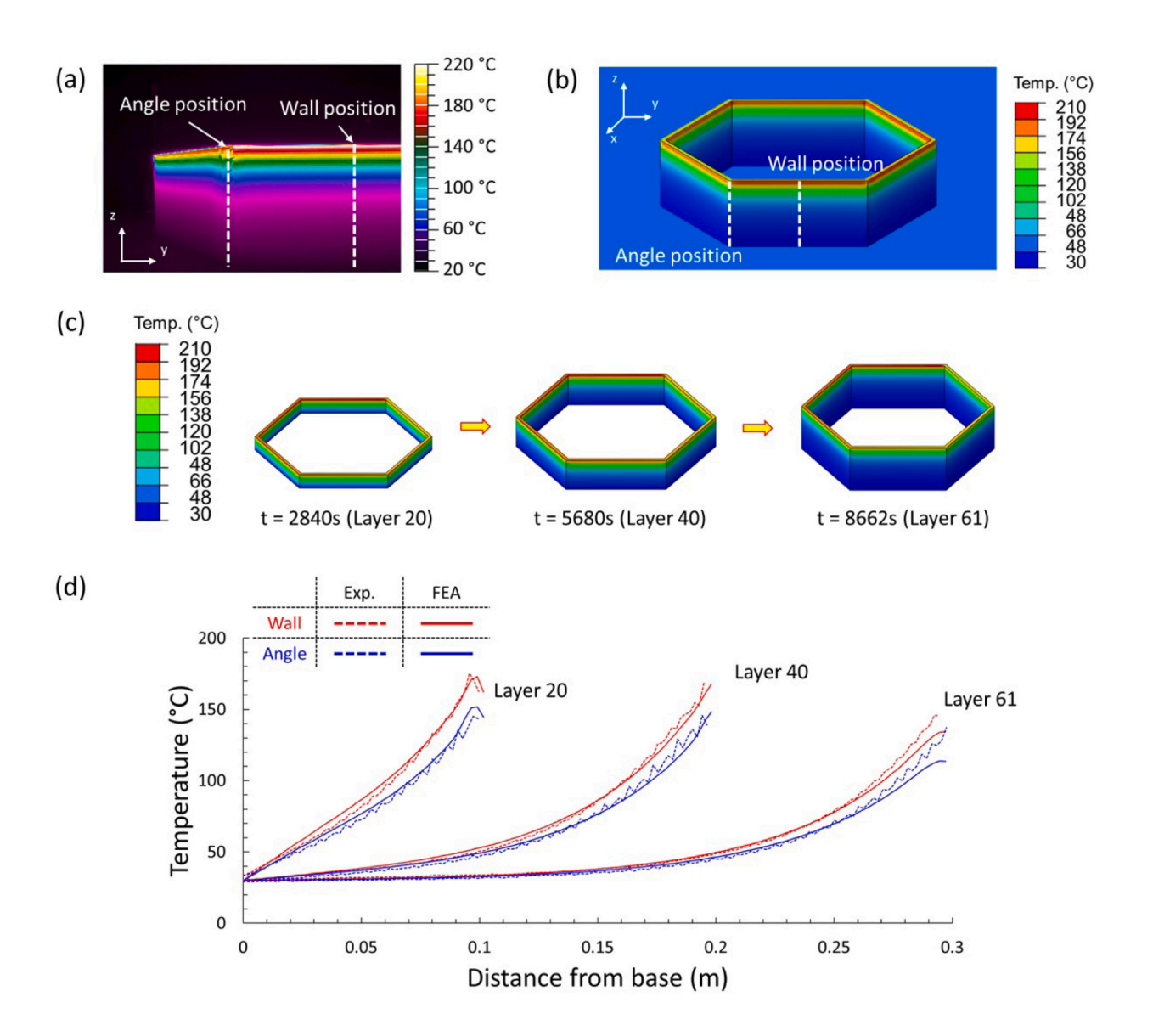


Fig. 6. FEA simulation model verification with experiment results (a) field of view in the experiment, (b) field of view in the simulation, (c) process of progressive material activation, and (d) comparison of temperature profiles of hexagon shape prints from FEA simulation (solid line) with those from experiment results (dashed line) at three different process time at the wall (red) and the angle position (blue). (For interpretation of the references to color in this figure legend, the reader is referred to the web version of this article.)

Table 3
Input parameters.

Variable name	Value
Variable lialile	value
Thermal conductivity, κ [W/m K]	0.27
Density, ρ [kg/m ³]	1470
Convection coefficient, h_{cv} [W/m ² K]	4
Emissivity, ϵ	0.9
Stefan–Boltzmann constant, σ [W/m ² K ⁴]	5.67×10^{-8}
Deposition temperature, T_{dep} [°C]	210
Ambient temperature, T_{env} [°C]	30
Bed temperature, T_{bed} [°C]	50
Layer Height, ∆I, [mm]	5.08
Thickness, w, [mm]	20.32

internal heat transfer of the printed layer occurs through conduction and the printed layer experiences heat loss through convection and radiation. The partial differential equation is converted into a recurrence relation with finite differences. The first derivative becomes,

$$\frac{dT}{dt} \simeq \frac{1}{\Delta t} (T(l, t + \Delta t) - T(l, t)) \tag{3}$$

The second derivative becomes,

$$\frac{\partial^2 T}{\partial l^2} \simeq \frac{1}{\Delta l^2} (T(l - \Delta l, t) - 2T(l, t) + T(l + \Delta l, t)) \tag{4}$$

The model has four sets of boundary conditions according to the position and stacking condition, as shown in Fig. 8. In the first case, Fig. 8(a), the first layer is deposited on the heated bed, which has a constant temperature. The layer has three free surfaces $(A = w + 2\Delta I)$ and one conduction surface with the base. In the second case, Fig. 8(b), the bottom layer becomes the middle position layer with the upper layer

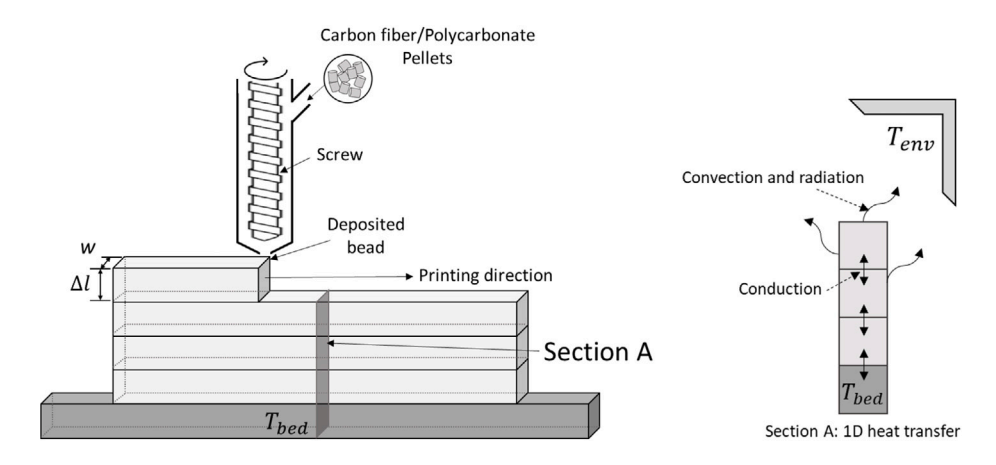


Fig. 7. Schematic of the large-scale additive manufacturing process with polymer extrusion and Section A: heat transfer via conduction, convection, and radiation in the 1D thermal model.

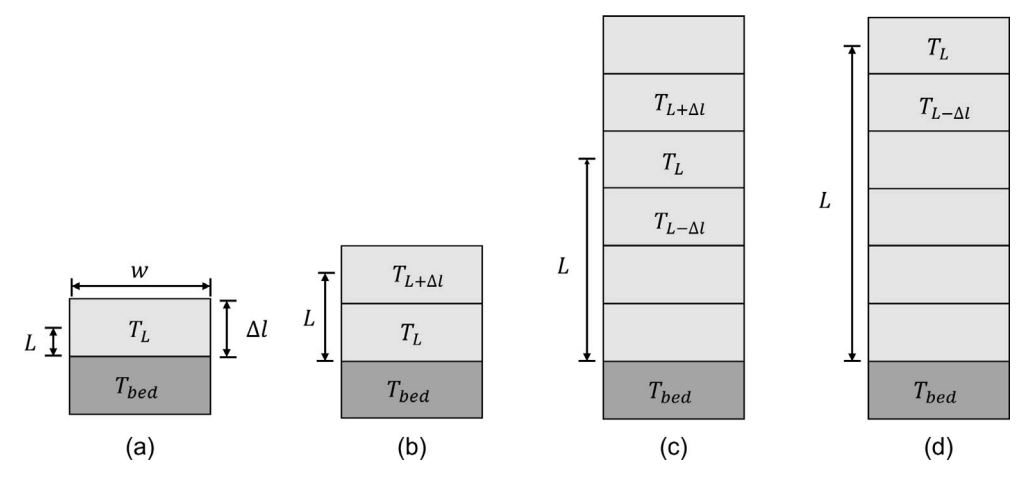


Fig. 8. Possible boundary condition cases during the additive manufacturing process (a) bottom node in the surface layer, (b) bottom node in the middle layer, (c) middle layer, and (d) top layer.

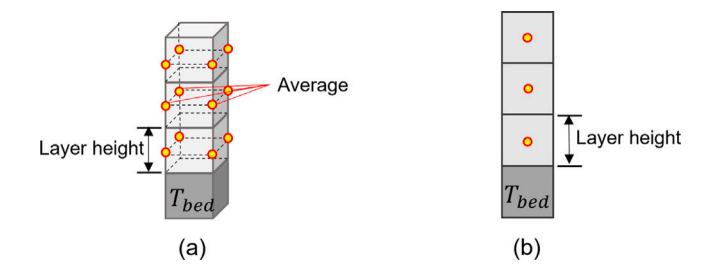


Fig. 9. Temperature extracting positions for (a) the FEA 3D simulation and (b) the reduced 1D heat transfer model.

and the base. So, it has two free surfaces (A=2dI), one conduction surface with the base and one conduction surface with the upper layer. In the third case, Fig. 8(c), the layer is located in the middle of two layers. It has two free surfaces for convection and radiation (A=2dI), and two conduction surfaces with upper and lower layers. For the last condition, Fig. 8(d), the top layer is the lastly deposited, and it has three free surfaces (A=w+2dI) and one conduction surface with a lower layer. Substituting Eqs. (3) and (4) into Eq. (1), the new temperature $T(I, t+\Delta t)$ can be solved for each of the possible boundary condition sets, as shown in Eq. (5). The stability of the numerical solution is ensured

by the Von Neumann stability criterion in Eq. (6).

$$T(l,t+\Delta t) = \begin{cases} T(L,t) + \frac{4\kappa\Delta t}{\rho C_{\rho}\Delta l^2} (T_{env} - T(L,t)) - \frac{\Delta t}{\rho C_{\rho}L\Delta l} Q_{out} & \text{, bottom/surface} \\ T(L,t) + \frac{4\kappa\Delta t}{\rho C_{\rho}\Delta l^2} (T(L-\Delta l,t) - T(L,t)) \\ + \frac{\kappa\Delta t}{\rho C_{\rho}\Delta l^2} (T(l+\Delta l,t) - T(l,t)) - \frac{\Delta t}{\rho C_{\rho}L\Delta l} Q_{out} & \text{, bottom/middle} \\ T(L,t) + \frac{\kappa\Delta t}{\rho C_{\rho}\Delta l^2} (T(L-\Delta l,t) - 2T(L,t)) + T(l+\Delta l,t) \\ - \frac{\Delta t}{\rho C_{\rho}\omega L l} Q_{out} & \text{, middle} \\ T(L,t) + \frac{\kappa\Delta t}{\rho C_{\rho}\Delta l^2} (T(L-\Delta l,t) - T(L,t)) - \frac{\Delta t}{\rho C_{\rho}\omega L l} Q_{out} & \text{, top} \end{cases}$$

 $\frac{\alpha \Delta t}{(\Delta l)^2} \le \frac{1}{2},$ $\alpha = \kappa / c_n \rho.$ (6)

(5)

A comparison between the experiment, the simulation, and the 1D heat transfer model is conducted. Fig. 9 shows the temperature extracting positions for each case. In the simulation results, temperature data at 4 points in the center of a layer are extracted, and an average value is used as an element temperature, Fig. 9(a). Element height is designed as half of a layer height to capture the center temperature of a layer and reduce the error caused by a nodal mass in the FEA simulation. In the 1D heat transfer model, temperature data are extracted at the center of an element, Fig. 9(b). The temperature profile comparison results at three different process times are shown in Fig. 10. Also, a comparison at a fixed position is conducted, and the results are shown in Figs. 11

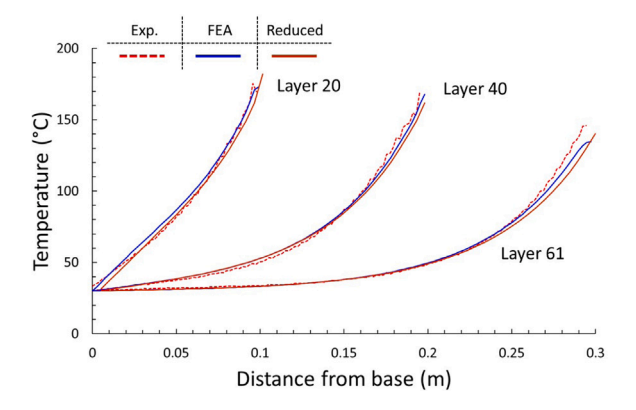


Fig. 10. Comparison of temperature profiles of hexagon shape print from the experiment (red dashed line), FEA simulation (blue solid line), and reduced model (brown slid line) with those from the experiment at wall position when 20, 40, and 61 layers are deposited. (For interpretation of the references to color in this figure legend, the reader is referred to the web version of this article.)

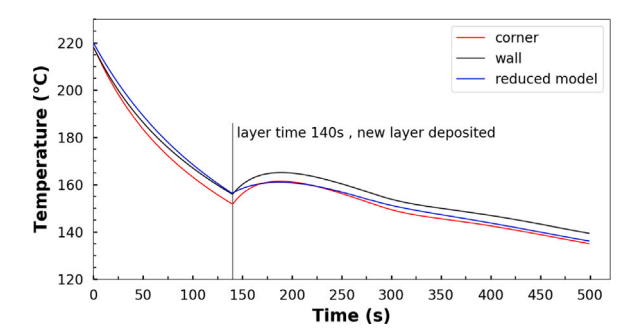


Fig. 11. Comparison of element temperature of the hexagon shape print from FEA simulation with that from the reduced (laver 50).

and 12 on different geometries. There is a temperature bounding when a new layer is deposited on the fixed position. The developed 1D model shows a good agreement with the simulation result at the wall position. However, the 1D model cannot capture the temperature difference between the wall and angle positions. Therefore, we analyze spatial variances of the temperatures to account for the effect of the corner.

4.3. Variance addition

The element temperature predicted by the 1D heat transfer model considers several physical parameters, while the geometric influences are ignored due to the simplification. Therefore, the cooling process is consistent for all positions on the layer, and it is not affected by printing shapes. The 1D heat transfer model will provide one predicted temperature cooling curve, which can be considered as only one position on the entire layer. This result is reasonable for wall geometry but not for geometries with corners. In layer printing, the temperature changes differently between straight walls and corners due to the variant contact surface area. Node positions at corners should have a higher or lower temperature, which is shown by the experiment results and the FEA simulation in Fig. 6.

By considering the complexity of geometry in reality manufacturing, making some adjustments for the temperature prediction results are necessary. As known, the FEA simulation behaves with good prediction performance with various geometries; hence, the temperature-changing curves between different positions on an entire layer generated from the FEA simulation are analyzed. The variances of temperatures among all positions at each timestamp are extracted from the corresponding

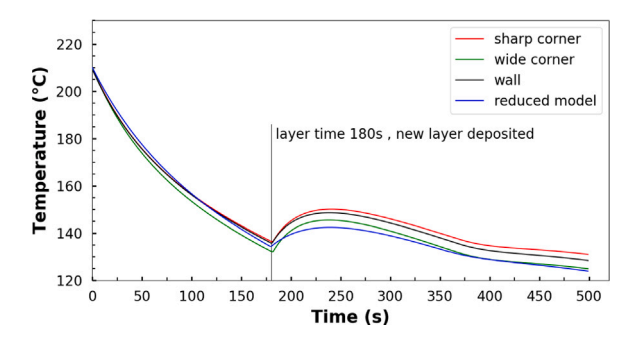
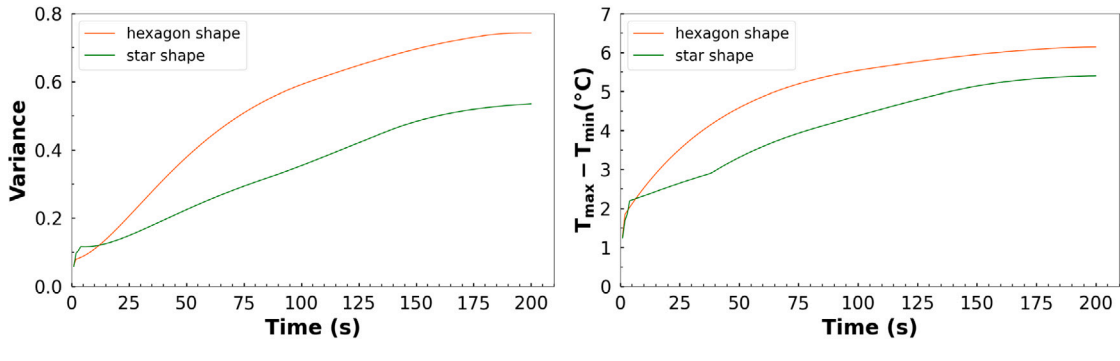


Fig. 12. Comparison of element temperature of the star shape print from FEA simulation with that from the reduced model (layer 50).

geometry simulation data. As shown in Fig. 13(a), the x-axis is recognized as the local layer time instead of the global layer time, and the y-axis is the temperature variances, which keeps increasing over time. Because the local layer time is applied here, the temperature cools as the x-axis timestamps go up. Therefore, the variance values are lower when the temperature is high and higher when the temperature is low. The hexagon geometry has all wide corners 120°; the star geometry comes with 36° sharp corners and 108° wide corners. According to the positions on the entire layer, the temperature variance for one type of corner hexagon shape is slightly lower than that in two types of a corner star shape in the first 10 s printing. After that, the temperature variance in the Hexagon geometry grows faster, and it is around 0.75, which is higher than a 0.5 variance in the star geometry after the 200 s. In order to explore the effect of corners, variances of the temperature from the whole structure and wall positions are compared under both hexagon shape and star shape. The wall positions are determined by excluding the corner positions where defined as a normalized distance of four times the printing bead width from the edges. According to Fig. 14(a) and (b), the temperature variance of a wall position, denoted by the blue line, starts to drop gradually after a 5 s printing, and it is near zero after the first 25 s, which is trivial. However, the temperature variance of the whole structure, represented as a red line, rises all the time, and it increases more significantly in the hexagon shape, which means that corners positively influence the variance of layer temperature change. Because sharp corners in star geometry cool like a wall over time, as shown in Fig. 12, the differences in temperature cooling rates between corner and non-corner positions will be more evident as corner degrees widen. In addition, denote T_{max} and T_{min} as the highest and lowest layer temperature at a time, respectively. Based on the FEA simulation data, Fig. 13(b) shows that the temperature differences between T_{max} and T_{min} under the hexagon shape case and star shape case match with the change of temperature variances. The smallest temperature difference is around 1.5 °C at the initial deposition time, and it increases to a stable value of 6 °C for the hexagon geometry and a stable value of 5 °C for the star geometry.

Therefore, to generate the final prediction data as accurately as the FEA simulation data, more than the 1D heat transfer model is needed, and it is reasonable to construct more sample data by considering the properties of corners. Here, a hybrid prediction model is proposed. We consider the corner property as variances based on the cooling data from an initial simulation, and the normal distribution is applied at each timestamp to collect more temperature samples. In the hybrid prediction model, the predicted temperature obtained from the 1D heat transfer model is set as a mean value, and variance extracted from the FEA simulation is added by timestamps as the variance value. Then, normalized random samples are able to be generated at each timestamp, so we have multiple temperature cooling curves as variate positions on an entire printing layer. Fig. 15 shows temperature cooling curves of this hybrid prediction and the FEA simulation on the top



- (a) Comparison of temperature variances
- (b) Comparison of temperature difference

Fig. 13. Temperature comparisons among all positions for top layer on hexagon shape and star shape based on the FEA simulation.

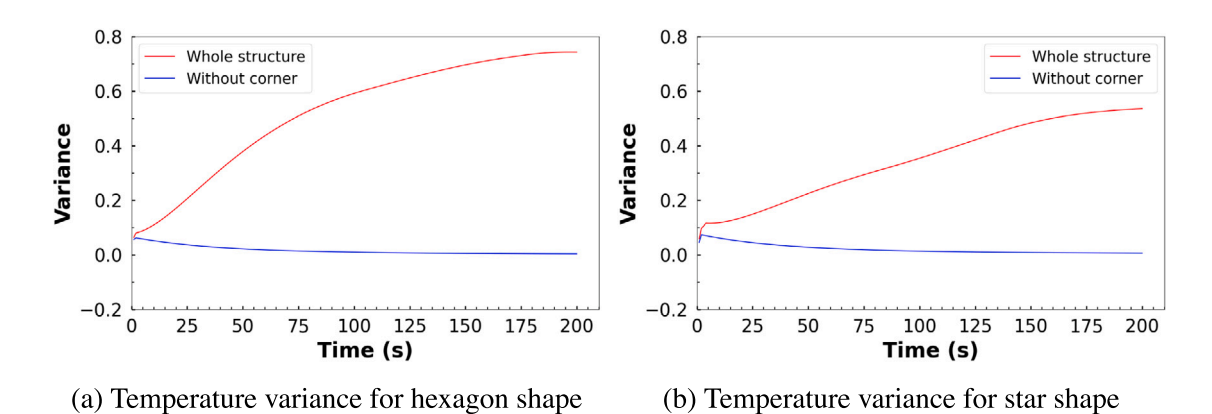


Fig. 14. Comparisons of the temperature variances from the whole structure and the wall position (excluding the corner) based on the FEA simulation (top layer). (For interpretation of the references to color in this figure legend, the reader is referred to the web version of this article.)

layer. After a duration of layer time 140 s, the temperature is in a range of 157.28 °C to 151.40 °C in the FEA simulation, and the temperature from the hybrid prediction cools to a range from 158.18 °C to 153.87 °C. In Fig. 16, temperature ranges are compared between the FEA simulation and the hybrid prediction over time. The temperature ranges highly overlap after a 100 s cooling. In addition, on each timestamp, a Kullback–Leibler divergence for the hybrid prediction distribution is calculated by setting the FEA simulation distribution as the benchmark. Kullback–Leibler divergences among timestamps in 140 s layer time are from the lowest 0.02 to the highest 1.71, which are very close to 0. Therefore, it is confident that the hybrid prediction model can mimic various temperatures of the FEA simulation well.

With the proper predicted temperature data, we are able to find the optimal layer time. The entire layer time can be divided into printing and waiting times. As stated in the experimental design, the printing time is 84 s for the hexagon geometry, and it is fixed, so we control the time after the printing time. Therefore, the tiny prediction difference after 100 s hardly influences the accuracy of the final optimization result. The structured layer time optimization model can monitor temperatures of multiple positions on an entire layer and find the optimal layer time that considers both product quality and production efficiency. Due to this function, the accuracy of the predicted temperature range is more important than single temperature values. Hence, the hybrid prediction model allows the offline design of layer time optimization.

5. Layer time control

As discussed, a layer's surface temperature closely influences the product quality and manufacturing efficiency in large-scale additive

manufacturing. Overheated and overcooled surfaces will cause deformation, cracking, and delamination issues. The product defects can be efficiently reduced when the layer temperature is controlled within the range from the lower bound T_l to the upper bound T_u and very close to the best temperature T_b . In order to guarantee the product quality, temperatures of multiple positions on the layer will be monitored. Therefore, an optimal layer time control model based on predicted temperature is applied. Because the predicted temperature from Section 4 is element temperature instead of surface temperature, the 156 °C element temperature corresponding to the surface temperature of 145 °C will be used as the best temperature.

5.1. Model for layer time optimization

Let M represent the number of positions being monitored. The temperature change of the ith location, for $i=1,2,\ldots,M$, is modeled by physics-based activation equations and variance adjustments in Section 4. The time t is known as the 1 s timestamp in the case study, which is a positive integer, in the following case study section; t for predicted element temperature at the tth position $\hat{T}^i(t)$ starts with time 0 when thermoplastic material is deposited at the tth position. The time 0 is also known as the activation of nodes in the FEA simulation. The less timestamp gap, the more accurate and stable optimal result will be given. The optimization model with integer decision variable t is built as follows:

$$\min_{t} \quad f(t) = \sum_{i=1}^{M} \omega_{i} (\hat{T}^{i}(t) - T_{b})^{2} + \omega_{0} t$$
 (7)

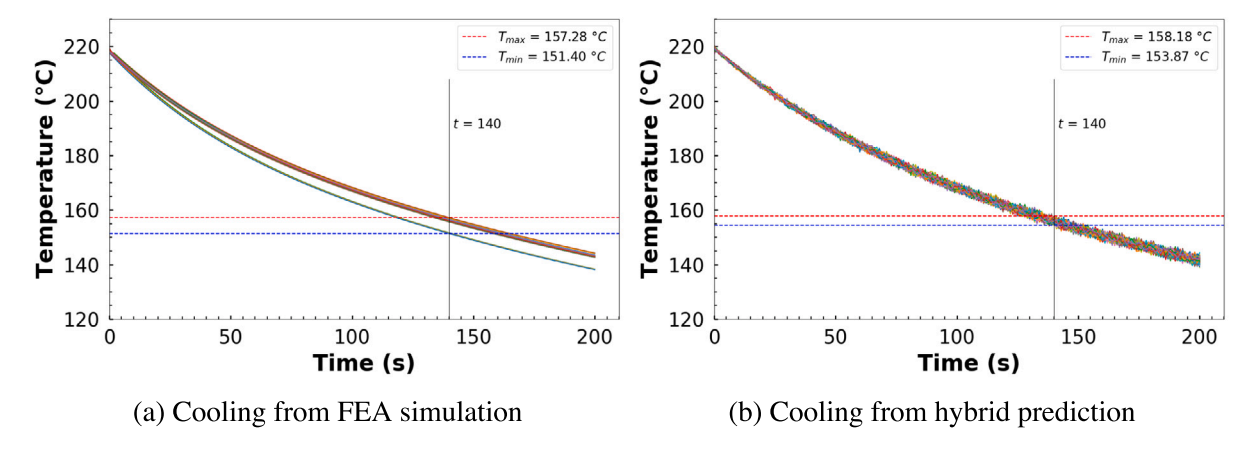


Fig. 15. Temperature cooling curves for FEA simulation and hybrid prediction based on hexagon shape (top layer).

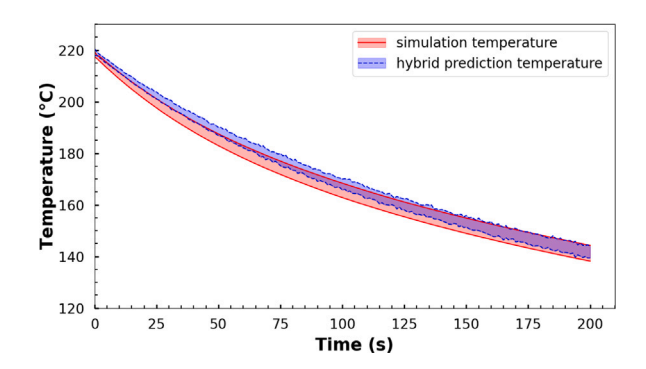


Fig. 16. Comparison of temperature cooling curves between FEA simulation and hybrid prediction for hexagon shape.

s.t.
$$\hat{T}^i(t) \ge T_i$$
, for $i = 1, 2, ..., M$
 $\hat{T}^i(t) \le T_u$, for $i = 1, 2, ..., M$
 $t \in \mathbb{Z}^+$

$$(8)$$

In the objective Eq. (7), f(t) is calculated as a weighted summation with the weight for each term denoted by ω_i , for $i=0,1,\ldots,M$. Here, a trade-off between the importance of temperature difference for each node position and the layer time will be considered by the weight ω_i . The first part of the objective function $\sum_{i=1}^M \omega_i (\hat{T}^i(t) - T_b)^2$ represents how close a position's element temperature is to the target temperature $T_b(156~^{\circ}\text{C})$. The second term $\omega_0 t$ considers the weight of layer time. By combining both terms, getting more minor differences between element temperature and target temperature among positions and minimizing layer time can be considered simultaneously by minimizing the objective function.

There are three constraints in Eq. (8). The first constraint ensures that all positions have an element temperature higher than the given lower temperature bound T_l (140 °C) at time t. Similarly, the second constraint guarantees that no position can have a layer temperature greater than the upper temperature bound T_u (165 °C) at time t. The last constraint regulates the layer time t to be positive integers as it represents timestamps. The reorganized feasible region of layer time t, denoted by $[t_l, t_u]$, can be obtained as follows:

$$\begin{aligned} t_{l} &= \max_{t} \{ \hat{T}^{i}(t) = T_{u}, t \in \mathbb{Z}^{+} \} \\ t_{u} &= \min_{t} \{ \hat{T}^{i}(t) = T_{l}, t \in \mathbb{Z}^{+} \} \end{aligned} \tag{9}$$

The layer time optimization model can be solved by minimizing the objective function f(t) over bounded decision variable interval $[t_l,t_u]$ by using the Sequential Quadratic Programming (SQP) method [9].

5.2. Iteration based solution approach

Even though the above optimal control model provides an optimal layer time under each case, it may not be the final result due to the cooling rate that varies under cases with different layer deposition times. As tested in the optimal control model between simulation cases with variate layer deposition time [10], the optimal layer time tends to decrease when the given layer time of simulation increases. When the layer deposition time is longer, the topside surface temperature of the layer is cooler. At the time a new layer is printed onto this cooler surface, the temperature cooling rate of the new topside layer will increase; then, the optimal control model will generate a shorter optimal layer time and vice versa. Finding optimal layer time is a dynamic process with a trend of convergence. Therefore, the final optimal layer time can be generated when it is equal to the layer deposition time of the simulation.

Based on the above findings, an adjusted iteration method is constructed, and the process framework is shown in Fig. 17. Denote τ^k , t^k , for k = 0,1,2..., as the layer deposition time in kth iteration and the relative optimal layer time in kth iteration, respectively. The process will start with an initial layer deposition time τ^0 , which is the input parameter of the 1D heat transfer model. By utilizing the temperature values predicted based on the layer deposition time τ^0 , an optimal result t^0 for the 0th iteration is obtained from the optimization model. If this value is not equal to the layer deposition time, a new iteration will start, and we use t^0 to update the τ^0 as the value of τ^1 . In each iteration of this framework, the optimal control model will provide an optimal layer time t^k based on the temperature cooling data generated by the 1D heat transfer model and adjusted by variances extracted from an initial FEA simulation with the layer deposition time τ^k . Then, comparing whether the given τ^k is different from t^k . If the layer time converges, the final recommended optimal layer time t^k is found. Otherwise, the k+1th iteration process begins, and the layer deposition time τ^{k+1} will be updated by the deposition time based optimal result t^k ; the temperature prediction and optimal time control processes will be applied iteratively until the layer deposition time equals optimal layer time. The converged layer time is the final optimal layer time for the printing process. Based on the hexagon shape, three iteration processes starting with different initial $\tau^0 = 90$ s, 130 s, and 200 s are shown in Fig. 18. The x-axis is the time(s), and the y-axis is represented by $\tau^k - t^k$ (s), which is the difference between the layer deposition time and its optimal layer time in the kth iteration. When this value equals zero, a convergence is achieved. After several iterations, the final optimal layer time under those three scenarios converges to the same number, 139 s.

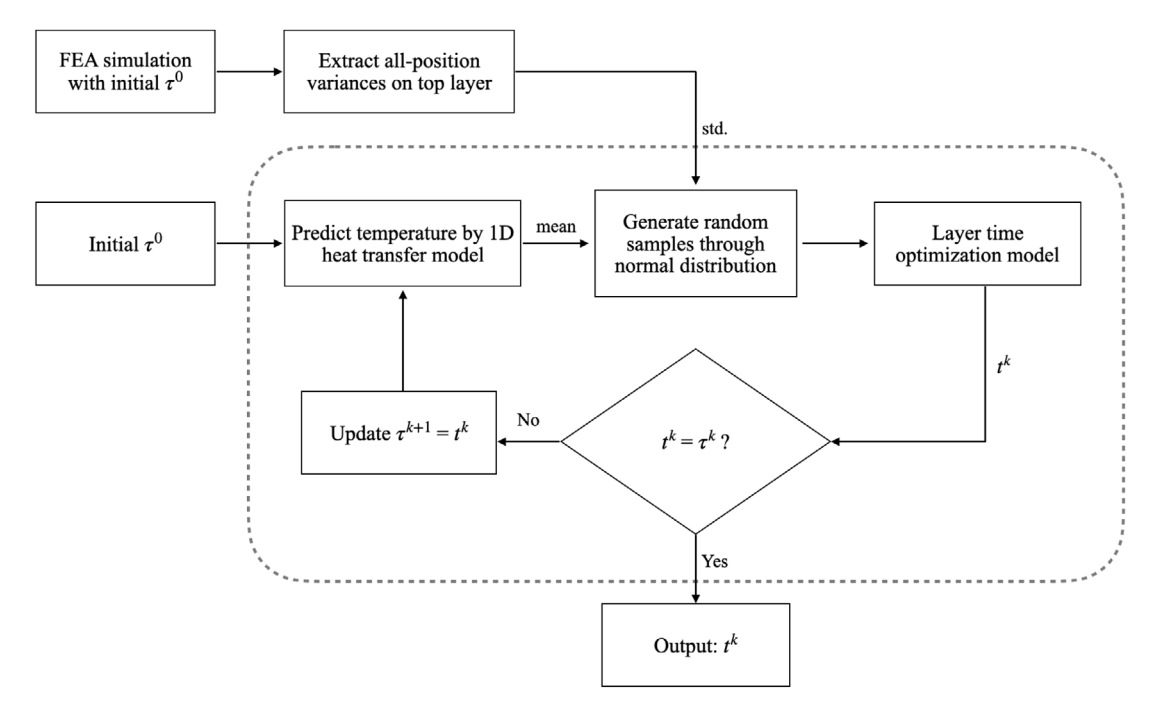


Fig. 17. Flowchart of the iteration based solution approach.

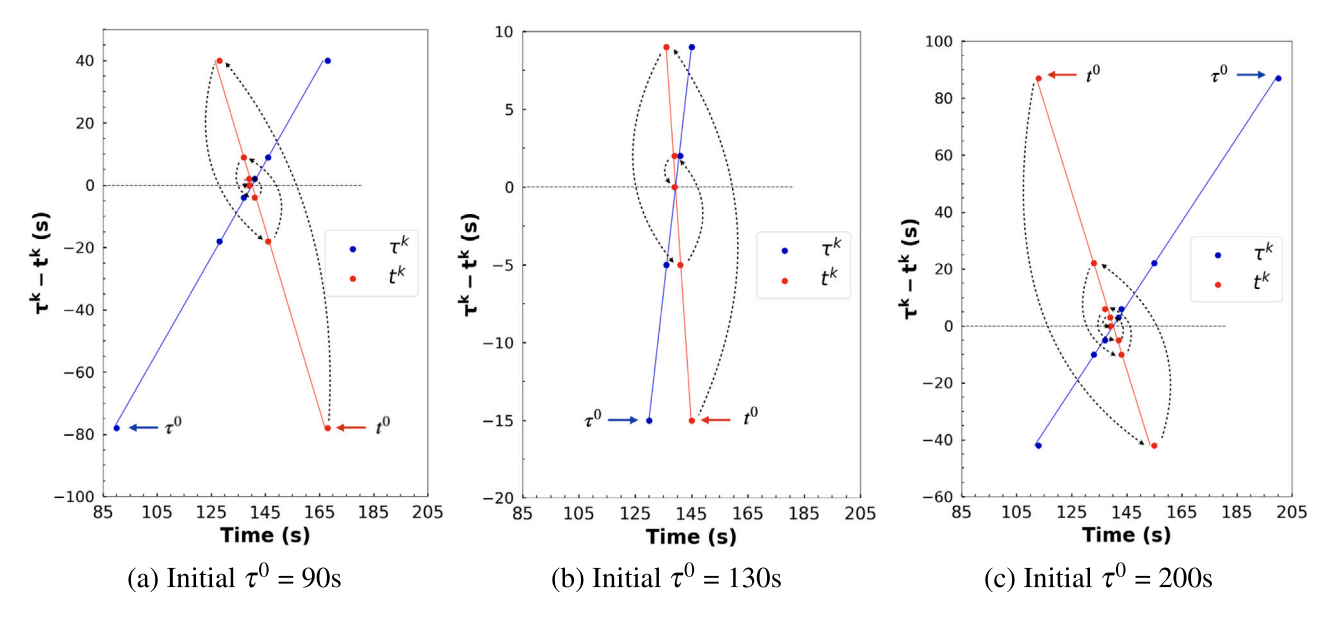


Fig. 18. Convergence of the optimal layer time for hexagon geometry with different initial layer deposition time τ^0 .

6. Case studies

Two cases with different printing geometries are tested to show the performance of the physics-based layer time optimization model. In order to verify the accuracy of the best optimal layer time for each case, the corresponding simulation data with a given layer deposition time is generated. An optimal result based on the simulation should be very similar to the best optimal layer time given by the model described in Sections 4 and 5.

6.1. Hexagon shape

A simple case based on layer 61, the topside, of the hexagon geometry is considered. First, the proposed hybrid model is applied to predict the layer temperature. Starting with the 1D heat transfer model

and predicting the element temperature, the initial layer deposition time is set to be 130 s with the deposition temperature of 220 °C; then, a generalized temperature cooling dataset with 61 layers is predicted. Next, variances extracted from a 130 s FEA simulation are added to the above-generalized dataset to show angle properties. In the initial simulation of this case, all positions on the layer are monitored except the first printed position and the last deposited node. The position printed first shows temperature anomaly and is ignored due to extra heat affection from the coming extrusion. A 1 s timestamp is used in this case. For the timestamp range from 0 to 200, temperature variances among monitored positions at each timestamp are observed from the simulation with 130 s layer deposition time. Table 4 analyzes a description of element temperature on layer 61 by mean and standard deviation.

 Table 4

 Description of element temperature among positions over time on layer 61 (Hexagon).

Timestamp (1 s)	0	1	 199	200
Position count	156	156	 156	156
Mean	218.429	217.857	 144.689	144.496
std	0.509	0.236	 0.857	0.857

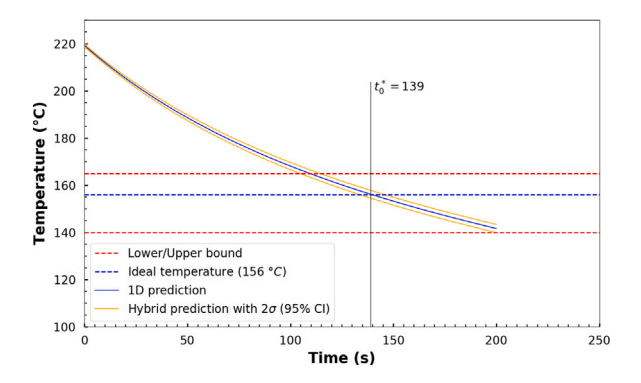


Fig. 19. Final optimization result on 1D model of hexagon shape with layer deposition time = 140 s. (For interpretation of the references to color in this figure legend, the reader is referred to the web version of this article.)

In order to simulate temperature cooling curves of different positions on the layer, more random samples of temperatures need to be generated by a normal distribution on each timestamp. Because the temperature predicted by the 1D heat transfer model is viewed as an average element temperature for positions on the layer, it is reasonable to set this temperature cooling data as the mean value at each timestamp. Therefore, random cooling samples as 150 positions are structured from a normal distribution with the above mean and variance. Besides, the coefficients ω_i , for $i = 0,1, \dots, 150$, in the optimal control model are all equal to 1. The above processes will iterate until the optimal results and layer deposition time converge. The final optimal result given by this paper dithers between 139 s and 140 s. In this situation, the optimal layer time is 140 s based a 139 s temperature prediction data; a 139 s optimal layer time is given by the 140 s prediction data. A single converged result is not obtained for two main reasons. First, the variable timestamp t, put in the optimal model, is positive integer values instead of continuous numbers, so the optimal output is susceptible to temperature values. Second, the randomly added variance values increase the sensitivity of layer time result in each time rerunning the program, which causes the final result to dither between two adjacent timestamps. Even though there is not a single converged layer time result, the final optimal layer time is narrowed down to a tiny range, and only two choices are needed to be verified to get the final suggestion when the timestamp is large, for example a 5 s timestamp. In our case study, because a 1 s timestamp is used and the difference between optimal results is very small, we assume that the results converge to the smaller value when the difference is less than 1 s. Therefore, the best optimal layer time given by the developed model is 139 s, which is shown in Fig. 19. The temperature curves are drawn based on temperature data predicted from the hybrid model. The solid blue line represents the temperature curve predicted by the 1D heat transfer model, and the two temperature cooling curves in the orange color are lines adjusted by adding variances with 95% confidence level.

A test based on the FEA simulation data shown in Fig. 20 verifies the optimal results given by developed approaches in this paper. The element temperature of simulation cooling data is extracted for comparison reasons, and the position of a node defined as element temperature in the hexagon simulation is shown in Fig. 9. The element temperature

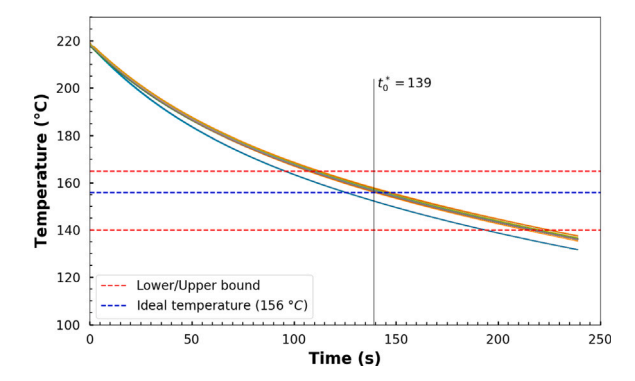


Fig. 20. Verified optimal layer time on hexagon shape simulation with layer deposition time = 139 s. (For interpretation of the references to color in this figure legend, the reader is referred to the web version of this article.)

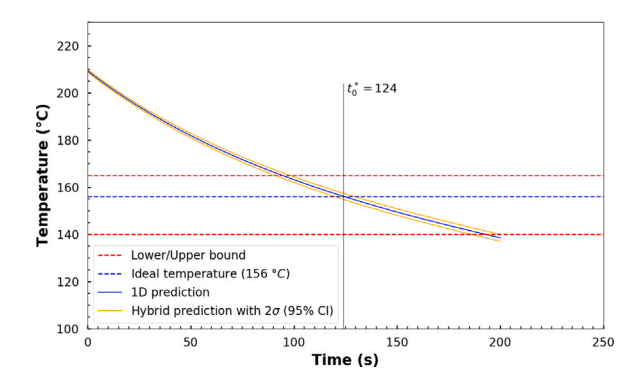


Fig. 21. Final optimization result on 1D model of star shape with layer deposition time = 124 s.

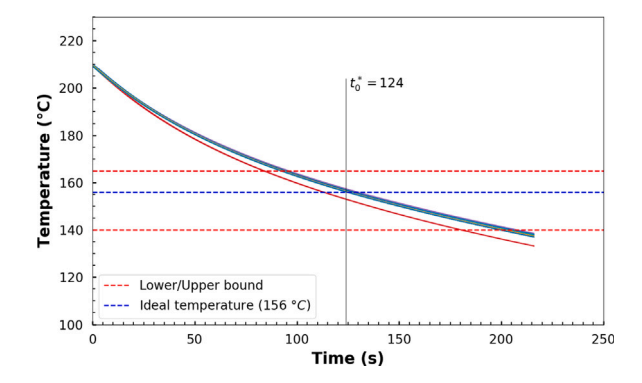


Fig. 22. Verified optimal layer time on star shape simulation with layer deposition time = 124 s.

cooling curves in Fig. 20 are shown by uniting the start printing time of positions in hexagon simulation with 139 s layer time. The *y*-axis is the element temperature (°C) on a layer, and the *x*-axis is the layer time (s). With the lower bound (140 °C)/upper bound (165 °C) shown in the red dashed line and target temperature (156 °C) described as the blue dashed line, the element temperature for each position cools down to around 156 °C as the vertical line t_0^* marks the optimal layer time = 139 s, which is the same as its layer deposition time.

6.2. Star shape

The star geometry is a more complex case than the hexagon shape. As described in Section 3, the star shape experimental design comes with 36° sharp corners and 108° wide corners instead of single type

Table 5

Description of element temperature among positions over time on layer61 (Star).

Timestamp (1 s)	0	1	 199	200
Position count	71	71	 71	71
Mean	209.188	208.511	 131.868	131.668
std	0.255	0.242	 0.731	0.732

120° corners in the Hexagon case. First, the element temperature of the star geometry is extracted by a dictionary of coordinates from initial simulation data with 180 s layer time. Two specific element positions of sharp corners are removed as outliers due to the design difference between the real 3D print and the FEA simulation. In the 1D heat transfer model, the initial layer deposition time matches our initial simulation case, which is 180 s; the deposition temperature is 210 °C for the start geometry. Then the same process as in Section 6.1 is applied. The element temperature of 71 positions is considered, and the standard deviation for this case is shown in Table 5.

With all coefficients $\omega_i=1$, the final optimal result given is a converged 124 s layer time, which is shown in the hybrid prediction model based Fig. 21. Fig. 22 verifies the result with a 124 s layer deposition time based on the FEA simulation data, and the vertical line t_0^* denotes the optimal layer time in this simulation case when the target temperature is (156 °C). Therefore, the best optimal layer time based on the star geometry is founded, which is 124 s, and this simulation verifies the model output given by the methods in this paper.

7. Conclusion

We propose an optimization framework to determine an optimal layer deposition time for the large-scale additive manufacturing process. With the determined optimal layer deposition times, successive layers are deposited on the surface, which has the proper layer temperature. In the optimization framework, a reduced physics-based activation model (the 1D heat transfer model) is used to predict the temperature history, substituting the time-consuming finite element analysis (FEA) and experiments. Temperature variances are extracted from a highfidelity FEA model to consider the geometric characters. The variances are used to generate the geometry-considered temperature data with the reduced model for different layer deposition times. An optimal control model is practiced to suggest a new layer deposition time, which is expected to have a proper surface temperature. The optimization process starts with a given initial layer deposition time and iterates until the predicted surface temperature converges to the target temperature. When the predicted surface temperature is the same as the target temperature, the optimization process stops and provides an optimal layer deposition time. The optimization process uses the reduced model for the iteration; thus, this process saves time for running complex simulations and the expensive costs of experiments.

The proposed optimization framework can be potentially improved in future works. First, the physics-based reduced model will be enhanced to predict the corner position temperature for reflecting geometry factor instead of extracting temperature variances from the FEA simulation model. Also, we only consider single-bead printing for the optimization model. Future work can be extended to study applicability of multi-bead printing. In addition, an optimization model which applies to the geometry with a non-homogeneous shape, without constant width and height, will be investigated in the future study.

CRediT authorship contribution statement

Lu Liu: Writing – original draft, Software, Methodology, Formal analysis, Data curation. **Eonyeon Jo:** Writing – original draft, Methodology, Investigation, Formal analysis, Data curation. **Dylan Hoskins:** Project administration, Data curation, Conceptualization. **Uday Vaidya:**

Supervision. **Soydan Ozcan:** Supervision, Project administration, Investigation, Funding acquisition. **Feng Ju:** Writing – review & editing, Project administration, Methodology, Investigation, Funding acquisition, Conceptualization. **Seokpum Kim:** Writing – review & editing, Supervision, Project administration, Funding acquisition, Data curation, Conceptualization.

Declaration of competing interest

The authors declare that they have no known competing financial interests or personal relationships that could have appeared to influence the work reported in this paper.

Data availability

The data that has been used is confidential.

Acknowledgments

The authors gratefully acknowledge support from the High-Performance Computing for Energy Innovation (HPC4EI) program and the HPC4Materials project sponsored by the Vehicle Technologies Office, Office of Energy Efficiency and Renewable Energy, U.S. Department of Energy. The research was also supported in part by the U.S. Department of Energy, Office of Energy Efficiency and Renewable Energy, Advanced Manufacturing Office, under contract DE-AC05-00OR22725 with UT-Battelle, LLC. The authors also appreciate the support from the National Science Foundation, United States, CMMI-1922739. The large-scale 3D printing system used in this work is LSAM®, developed by Thermwood Corp., and the system was operated by Local Motors for this work.

References

- A. Gebhardt, Understanding additive manufacturing: rapid prototyping rapid tooling - rapid manufacturing, Carl Hanser Verlag, Munich, Germany, 2012.
- [2] T.D. Ngo, A. Kashani, G. Imbalzano, K.T. Nguyen, D. Hui, Additive manufacturing (3D printing): A review of materials, methods, applications and challenges, Composites B 143 (2018) 172–196.
- [3] A. Bellini, L. Shor, S.I. Guceri, New developments in fused deposition modeling of ceramics, Rapid Prototyp. J. 11 (2005) 214–220.
- [4] C.E. Duty, V. Kunc, B. Compton, B. Post, D. Erdman, R. Smith, R. Lind, P. Lloyd, L. Love, Structure and mechanical behavior of big area additive manufacturing (BAAM) materials, Rapid Prototyp. J. 23 (2017) 181–189.
- [5] Thermwood, Large scale additive manufacturing, 2019, http://thermwood.com/ lsam/brochures/lsam2017brochure/index.html Last accessed on Jan. 16, 2019.
- [6] L.J. Love, Utility of Big Area Additive Manufacturing (BAAM) For The Rapid Manufacture of Customized Electric Vehicles, Technical Report, Oak Ridge National Lab. (ORNL), Oak Ridge National Lab. (ORNL), Oak Ridge, TN (United States), 2015.
- [7] B. Brenken, E. Barocio, A. Favaloro, V. Kunc, R.B. Pipes, Fused filament fabrication of fiber-reinforced polymers: A review, Addit. Manuf. 21 (2018) 1–16.
- [8] B.G. Compton, B.K. Post, C.E. Duty, L. Love, V. Kunc, Thermal analysis of additive manufacturing of large-scale thermoplastic polymer composites, Addit. Manuf. 17 (2017) 77–86.
- [9] F. Wang, S. Fathizadan, F. Ju, K. Rowe, N. Hofmann, Print surface thermal modeling and layer time control for large-scale additive manufacturing, IEEE Trans. Autom. Sci. Eng. 18 (1) (2020) 244–254.
- [10] E. Jo, L. Liu, F. Ju, D. Hoskins, D.K. Pokkalla, V. Kunc, U. Vaidya, S. Kim, The design of layer time optimization in large scale additive manufacturing with fiber reinforced polymer composites, in: SAMPE Technical Conference Program, 2022.
- [11] N. Mohan, P. Senthil, S. Vinodh, N. Jayanth, A review on composite materials and process parameters optimisation for the fused deposition modelling process, Virtual Phys. Prototyp. 12 (1) (2017).
- [12] B. Lee, J. Abdullah, Z. Khan, Optimization of rapid prototyping parameters for production of flexible ABS object, J. Mater Process. Technol. 169 (2005) 54–61.
- [13] X. Tian, T. Liu, C. Yang, Q. Wang, D. Li, Interface and performance of 3D printed continuous carbon fibre reinforced PLA composites, Composites A 88 (2016) 198–205.
- [14] N. Hill, M. Haghi, Deposition direction-dependent failure criteria for fused deposition modelling polycarbonate, Rapid Prototyp. J. 20 (2014) 221–227.

- [15] O.A. Mohamed, S.H. Masood, J.L. Bhowmik, Experimental investigations of process parameters influence on rheological behaviour and dynamic mechanical properties of FDM manufactured parts, Mater. Manuf. Process. 31 (2015) 1983–1994.
- [16] S.K. Everton, M. Hirsch, P. Stravroulakis, R.K. Leach, A.T. Clare, Review of insitu process monitoring and in-situ metrology for metal additive manufacturing, Mater. Des. 95 (2016) 431–445.
- [17] S. Berumen, F. Bechmann, S. Lindner, J. Kruth, T. Craeghs, Quality control of laser and powder bed based additive manufacturing (AM) technologies, Physics Procedia 5 (2010) 617–622.
- [18] F. Wang, H. Mao, D. Zhang, X. Zhao, Y. Shen, Online study of cracks during laser cladding process based on acoustic emission technique and finite element analysis, Appl. Surf. Sci. 255 (2008) 3267–3275.
- [19] J.E. Seppala, K.D. migler, Infrared thermography of welding zones produced by polymer extrusion additive manufacturing, Addit. Manuf. 12 (2016) 71–76.
- [20] S. Fathizadan, F. Ju, K. Rowe, A. Fiechter, N. Hofmann, A novel real-time thermal analysis and layer time control framework for large-scale additive manufacturing, J. Manuf. Sci. Eng. 143 (1) (2021).
- [21] S. Fathizadan, F. Ju, F. Wang, K. Rowe, N. Hofmann, Dynamic material deposition control for large-scale additive manufacturing, IISE Trans. 54 (9) (2022) 817–831.
- [22] B. Brenken, E. Barocio, A. Favaloro, V. Kunc, B.R. Pipes, Development and validation of extrusion deposition additive manufacturing process simulations, Addit. Manuf. 25 (2019) 218–226.

- [23] Y. Zhang, Y.K. Chou, Three-dimensional finite element analysis simulations of the fused deposition modeling process, Proc. Inst. Mech. Eng. B 220 (2006).
- [24] T. D'Amico, A.M. Peterson, Bead parameterization of desktop and room-scale material extrusion additive manufacturing: How print speed and thermal properties affect heat transfer. Int. J. Adv. Manuf. Technol. 34 (2020).
- [25] J.T. Owens, A. Das, M.J. Bortner, Accelerating heat transfer modeling in material extrusion additive manufacturing: From desktop to big area, Addit. Manuf. 55 (2022).
- [26] D. Hoskins, E. Barocio, D. Koester, D. Penumadu, V. Kishore, A.J. Thomas, W. Henken, J.A. Remirez, S. Kim, M. Ramirez, T. Smith, F. Mattingly, C.E. Duty, V. Kunc, Development of Large Scale Extrusion Deposition for Structural Applications, Technical Report, Institute for Advanced Composites Manufacturing Innovation (IACMI), IACMI, Knoxvill, TN, 37932, 2022.
- [27] A. Nycz, V. Kishore, J. Lindahl, C.E. Duty, C. Carnal, V. Kunc, Controlling substrate temperature with infrared heating to improve mechanical properties of large-scale printed parts, Addit. Manuf. 33 (2020).
- [28] V. Kishore, A. Nycz, J. Lindahl, C. Duty, C. Carnal, V. Kunc, Effect of infrared preheating on the mechanical properties of large format 3d printed parts, in: 2019 International Solid Freeform Fabrication Symposium, University of Texas at Austin, 2019.
- [29] ASTM.standard, Standard Test Method for Determining Specific Heat Capacity By Differential Scanning Calorimetry, ASTM International, West Conshohocken, PA. 2018.
- [30] L.J. Love, V. Kunc, O. Rios, C.E. Duty, A.M. Elliott, B.K. Post, R.J. Smith, C.A. Blue, The importance of carbon fiber to polymer additive manufacturing, J. Mater. Res. 29 (2014).